

Analytical Modeling of Industrial-Related Silicon Solar Cells

Tobias Fellmeth, Florian Clement, and Daniel Biro

Abstract—Fast and accurate simulation tools are key to increasing our understanding of silicon-based solar cells. A lucid graphical unit interface and experimentally obtained input parameters help make these tools accessible for a wide range of users. In this paper, we present a fast Excel tool based on the well-known two-diode model supporting conventional and metal-wrap-through cell architectures. The selective emitter approach, spatial varying emitter recombination, and optical simulations are taken into account. A set of consistent input parameters, including the emitter recombination in the passivated case, as well as the metal contacted for both idealities, are given as a function of the emitter sheet resistance. This set on input parameters is associated with industrial-related technologies for conventional and metal-wrap-through silicon solar cells.

Index Terms—Emitter, metal wrap through (MWT), modeling, solar cell.

I. INTRODUCTION

SIMULATION of silicon solar cells is of key importance for the whole photovoltaic industry. The different approaches can be classified into three different approaches, which differ in the degree of complexity.

The first approach uses 2-D and 3-D device simulations with software tools like Sentaurus [1], ATLAS [2], or Comsol [3]. A symmetric element of the device is defined and meshed in finite elements. Boundary conditions for the differential equations for holes and electrons lead to a convergent solution on these elements. Since this approach is based on fundamental device physics using the transport and continuity equations, the highest degree of accuracy can be expected. However, inherently dealing with such complex software consumes computer and labor time.

The second approach uses 3-D or pseudo-3-D network simulations. In the software tool SPICE [4], a mesh needs to be defined in which local diodes are linked with resistors. The physics of the minority charge carriers are described in the two-diode model by the dark saturation current densities j_{01} and j_{02} ¹ for each node. Within this approach, the spatial characteristics of a solar cell are still represented accurately in the simulation, yet the overall simulation procedure is less complex. Since the two-diode model is used, ray tracing is not necessary, and

no differential equations describing the minority charge carrier transport need to be solved, thus reducing the complexity of the simulation procedure. However, resistive effects caused by the majority charge carriers are still of the distributed kind and must be modeled in accordance with the Kirchhoff rules leading also to differential equations.

The last approach is referred to 0-D or 1-D modeling by using one global two-diode model with a lumped series resistance for the whole device. This approach leads to the approximation of a spatial constant junction voltage V_j that, in turn, leads to a spatial constant series resistance that only depends on device geometry and electrical properties such as metal resistivity or emitter sheet resistance. Computing time of such an approach lies in the range of seconds.

In this paper, the authors present an Excel-based tool named Gridmaster, for silicon solar cells using the third approach described above. The tool optimizes the front metal grid pattern of conventional solar cells exhibiting the “H-grid” pattern, as well as back contact metal wrap through (MWT) [5] solar cells. The following features are included:

- 1) the two-diode model;
- 2) graphical unit interface;
- 3) selective emitter structures;
- 4) recombination at emitter/metal interfaces;
- 5) modeling of concentrator solar cells.

II. EXCEL TOOL GRIDMASTER

A. Basic Work Principle

There is a fundamental tradeoff between light shading and electrical resistance in a solar cell with a metal grid on the light facing, or front side. Two quantities describe this tradeoff:

- 1) the photogenerated current j_{ph} that reaches its maximum when the metal coverage fraction F_M equals zero;
- 2) the series resistance r_s of the whole solar cell device that describes heat dissipation at an ohmic resistor, which reaches its maximum when F_M equals zero.

Therefore, a parameter needs to be found that relates F_M to r_s and j_{ph} .

The front-side² electrode of a conventional solar cell is based on a so-called H-pattern, which exhibits a parallel grid finger structure perpendicular to the broad busbars. Thus, the quantity of the screen-printed grid fingers n_f relates to $j_{ph} = j_{ph}(n_f)$ and $r_s = r_s(n_f)$ and, therefore, to the conversion efficiency η of the solar cell device. A typical graph exhibiting an optimum is shown in Fig. 1.

Manuscript received May 3, 2013; revised June 17, 2013, July 30, 2013, and August 23, 2013; accepted August 28, 2013. Date of publication September 30, 2013; date of current version December 16, 2013.

The authors are with the Fraunhofer Institute for Solar Energy Systems ISE, 79110 Freiburg, Germany (e-mail: tobias.fellmeth@ise.fhg.de; Florian.clement@ise.fhg.de; Daniel.biro@ise.fhg.de).

Digital Object Identifier 10.1109/JPHOTOV.2013.2281105

¹Variables using a “j” are always current densities and from now on will be denoted as currents only.

²Corresponds always to the illuminated side of the solar cell.

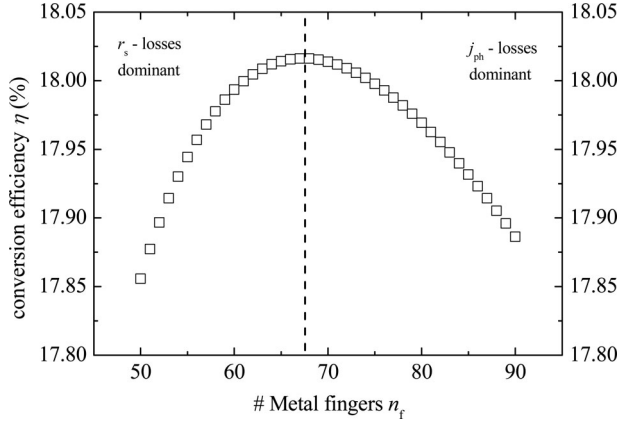


Fig. 1. n_f is a variable of j_{ph} and r_s , both of which affect the maximum power output of a solar cell device. Therefore, the conversion efficiency η is linked to n_f and reaches a maximum.

Due to the p-n junction of a solar cell the current–voltage characteristic follows an exponential law given by Shockley in 1949 [6]. During operation, the voltage at the p-n junction V_j is increased compared with the voltage between the external contact V due to the series resistance. Hence, the external voltage generated from the solar cell V in Shockley’s diode equation reads³ $V_j = V - r_s j$.

A deviation of the ideal diode characteristic was first mentioned by Sah *et al.* [7]. He pointed out that Shockley–Read–Hall recombination [8] induced by mid-gap defect states in the space charge region exhibits an ideality factor of 2. Therefore, at low voltage forward bias, the current–voltage characteristic can be mainly dominated by a diode with an ideality factor of $n = 2$. Finally, the two-diode model for an illuminated solar cell reads

$$j = j_{01} \cdot \left(e^{\frac{V - r_s j}{V_t}} - 1 \right) + j_{02} \cdot \left(e^{\frac{V - r_s j}{2 \cdot V_t}} - 1 \right) + \frac{V - r_s j}{r_p} - j_{ph} \quad (1)$$

where V is the voltage generated between the external metal contacts, V_t the thermal voltage, r_p the area weighted parallel resistance, $j_{01} = j_{01}(n_f)$ the global dark saturation current with an ideality factor of 1, and $j_{02} = j_{02}(n_f)$ the global dark saturation-current with an ideality factor of 2. The dark saturation currents can also depend on n_f when recombination is accounted for at the emitter-metal interface (j_{01}) and the space charge region underneath (j_{02}), respectively [9]–[12]. The equivalent circuit corresponding to the two-diode model is displayed in Fig. 2.

At given n_f , the input parameters for (1) are calculated as described later in the paper. The resulting I – V curve yields the short-circuit current j_{sc} , the open-circuit voltage V_{oc} , the fill factor FF , and the conversion efficiency η . By variation of n_f , a graph as shown in Fig. 1 is generated, where, in this case, an optimal balance between resistive, shading, and recombination

³In this case, the forward biased I – V curve is in the fourth quadrant; therefore, $j < 0$ for $V < V_{oc}$, and $r_s j$ needs to be subtracted from V . The sign in the exponent originates from the junction voltage V_j being higher compared with the external voltage V under illumination.

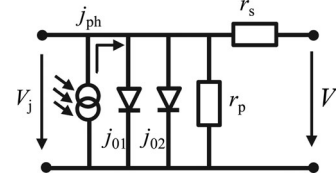


Fig. 2. Equivalent circuit diagram shows the two-diode model as implemented in Gridmaster. Two diodes with an ideality factor of $n = 1$ and $n = 2$ are incorporated.

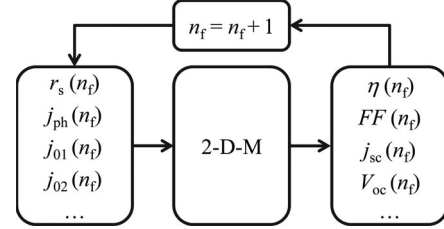


Fig. 3. Flowchart of the Excel-based software tool Gridmaster. j_{01} and j_{02} are the dark saturation currents from the diodes displayed in Fig 2. The lower and upper bounds of n_f are defined priori, resulting in a graph as displayed in Fig 1.

losses is found at $n_f = 67$. In Fig. 3, the flowchart visualizes the operating principle of the Excel-based tool “Gridmaster.”

B. Calculating the Total Series Resistance r_s

Every solar cell with a metal grid on one or both sides and a full-area emitter has at least four inherent contributions to the total series resistance r_s [13], [14]. These are the following:

- 1) r_B : current flow of charge carriers in the bulk;
- 2) r_E : lateral flow of charge carriers in the emitter;
- 3) r_c : contact resistance at the emitter–metal interface;
- 4) r_f : electron flow in the metal electrodes (grid).

It is common to distinguish between a series resistance that is generated from the front side r_{s_front} (emitter and metallization) which depend on n_f and from the bulk and rear side r_{s_rear} independently from n_f .

r_B and r_E occur within the semiconductor material and can depend on the injection level. A constant expression can only be found if the approximation of low-level injection holds at least up to the maximum power point voltage V_{mpp} . Usually, for industrial p-type solar cells, this condition is fulfilled [15].

Further contributions to the series resistance have to be taken into account, if the front busbars and the rear aluminum are contacted locally leading additionally to r_{BB} and r_{Al} , respectively. The transition resistance between the highly doped back surface field (BSF) and the eutectic Al-layer on the rear side can be neglected.

The MWT solar cell enables a higher conversion efficiency potential compared with the conventional H-grid design [16] although it exhibits additional contributions to r_s [17]. These contributions are as follows:

- 1) lateral current flow over the rear n-contact pads in the bulk r_L ;
- 2) current flow through the metal filled vias from the front to the rear side r_{via} .

In the MWT case, resistive losses occur in continuous metallic n -pads on the rear side and depend on the number of external contact pins. However, recent designs for the rear side of MWT solar cells have local pads [18], [19]. In this case, each pad is externally contacted, and lateral current flow in the metal is suppressed effectively. Hence, the contribution to the total series resistance can be neglected ($r_{BB} \sim 0$).

The derivation of r_s and its implementation in “Gridmaster” is shown in the Appendix.

C. Implementation of the Selective Emitter Approach

The selective emitter approach [20] combines a highly n^{++} -doped emitter underneath the front electrode and in the illuminated area a weaker doped emitter n^+ . This enables, simultaneously, a low contact resistance of the front electrode and a reduced Auger recombination in the n^+ -emitter, leading to a higher j_{sc} and V_{oc} potential.

The increased repelling of minority charge carriers from reaching the emitter–metal interface is a frequently underestimated effect of a selective emitter [21]. This effect is reflected in the dark saturation currents j_{0e-met} and j_{02-met} . The former complies with a diode ideality factor of $n = 1$ and the latter of $n = 2$. By area weighting the local dark saturation currents that share the same ideality factor, the effective dark saturation currents j_{01} and j_{02} are obtained [22]. Therefore, the global dark saturation current introduced in Fig. 2 in case of a diode with an ideality factor of $n = 1$ reads

$$j_{01} = j_{0b} + (1 - F_{n^{++}}) \cdot j_{0e-n^+} + (F_{n^{++}} - F_M) \cdot j_{0e-n^{++}} + F_M \cdot j_{0e-met}. \quad (2)$$

In addition, for the diode with an ideality factor of $n = 2$, the following expression holds:

$$j_{02} = (1 - F_M) \cdot j_{02-n} + F_M \cdot j_{02-met}. \quad (3)$$

j_{0b} denotes the dark saturation current of the bulk and the rear side, $j_{0e-n^{++}}$ the dark saturation currents of the weakly and highly doped emitter, respectively, $j_{0e(02)-met}$ the dark saturation currents of the metallized emitter, j_{02-n} the dark saturation current of the passivated emitter for the assumption that n^+ and n^{++} share the same j_{02} , and F the area fraction of the regarded j_0 .

The area-weighted addition of j_0 values requires a negligible variation of access charge carriers Δn between neighboring regions. A recent study from Greulich *et al.* [22] supports this approach for emitters with sheet resistances between 11 and 120 Ω/sq under standard test conditions.

Fig. 4 displays a cross section of a front grid finger contacting the selectively phosphorus-doped emitter. Although the metal electrode partly shades the n^{++} -area in this case, the dark saturation current is, by definition, unaffected by illumination. Hence, $j_{0e-n^{++}}$ is constant throughout the noncontacted shaded part of the solar cell device. The j_{02} value is assumed to be constant for the case of a passivated emitter. In Section III-C, this assumption is discussed in more detail.

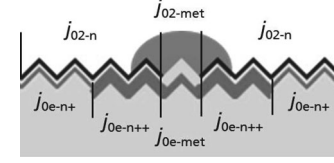


Fig. 4. Schematic cross section of a device featuring a selective emitter is shown that exhibits three areas represented by its dark saturation currents. In this case, a seed-layer provides the emitter–metal contact and subsequent silver or copper plating step generates the bulk finger.

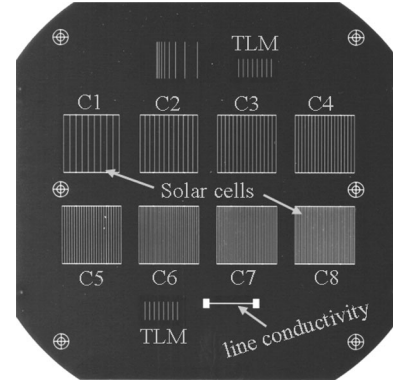


Fig. 5. Front view of a whole 5-in wafer is displayed. Eight individual solar cells are realized on one wafer (C1–C8). Additionally, support structures for characterization are incorporated.

III. INPUT PARAMETERS

For exact modeling, precisely measured input parameters are a mandatory requirement. In this section, a set of input parameters for “Gridmaster” are identified and presented. To this purpose, 2 cm \times 2 cm sized FZ-Si-based solar cells with printed front grid have been fabricated. A wafer featuring eight individual solar cells is shown in Fig. 5.

The cells feature a screen-printed metallization on both sides resulting in a full-area aluminum BSF on the rear surface. The emitter is generated by means of a thermal diffusion in a tube furnace. In order to reduce edge effects, the perimeter of each cell is embedded in a so-called emitter window.

A. Emitter Recombination

A method to determine the value of j_{0e-met} without the need of parallel processed lifetime samples has been published at the first SiliconPV [23]. The main idea features the determination of V_{oc} on actual solar cells with varying metallization fraction, as shown in Fig. 5. This value is sensitive to the emitter doping profile and front metallization and, therefore, to contact firing or annealing conditions.

For the passivated j_{0e-n^+} values, the common method for symmetrically processed lifetime samples introduced by Kane and Swanson [24] has been applied.

The implementation of the experimentally obtained dark saturation currents in Gridmaster results in a parameterization over the emitter sheet resistance R_{sh} according to Fig. 6.

The trends of the fitted curves are in good accordance with the existing theory [9]–[11] and can be explained by shifting

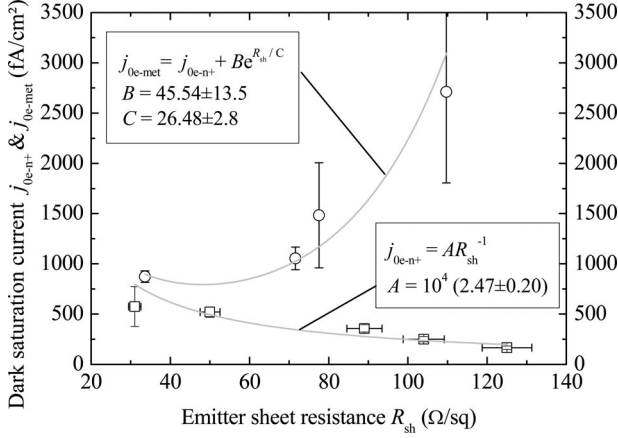


Fig. 6. Recombination currents for the metallized emitter j_{0e-met} and for the illuminated j_{0e-n+} are displayed. We fit the data to extract a dynamic model in dependence of the emitter sheet resistance R_{sh} .

regimes between volume and surface recombination in the highly doped region. The fit functions are chosen based on the physical behavior. In the passivated case, j_{0e-n+} vanishes for large R_{sh} . In the metallized case for low R_{sh} , the passivated and unpassivated converges and j_{0e-met} corresponds j_{0e-n+} . For high R_{sh} , the resulting j_{0e-met} value is dominated by the exponential term due to surface recombination at the emitter–metal interface.

Strictly speaking, the results presented in Fig. 6 are only valid for one screen-printed thick-film paste and emitter doping profile. Based on experience, however, we know that other thick-film pastes fired on optimal conditions reach similar values of j_{0e-met} on the respective emitter.

B. Recombination in the Bulk and at the Rear Side

In the case of highly doped regions existing in a solar cell device, it is common practice to describe recombination that exists in this region in the form of an effective surface recombination velocity S_{eff} or better in a characteristic dark saturation current j_0 independent of the bulk doping [25]. In the case of a full-area aluminum alloyed rear side, a guideline to extract j_0 can be found here [26].

The effective dark saturation current of the bulk and the rear side j_{0b} is obtained by linking recombination in the bulk and the rear side by means of a geometry factor G [25]:

$$j_{0b} = \frac{qDn_i^2}{N_A L_{Bulk}} \cdot \underbrace{\frac{\frac{S_{eff} \cdot L_{bulk}}{D} + \tanh\left(\frac{W}{L_{bulk}}\right)}{1 + \frac{S_{eff} \cdot L_{bulk}}{D} \cdot \tanh\left(\frac{W}{L_{bulk}}\right)}}_{G^{-1}} \quad (4)$$

whereby q denotes the elementary charge, D the diffusion coefficient of the minority carriers in the bulk, n_i the intrinsic charge carrier density in the bulk, N_A the acceptor density in the bulk, L_{bulk} the diffusion length in the bulk, and W the thickness of the bulk.

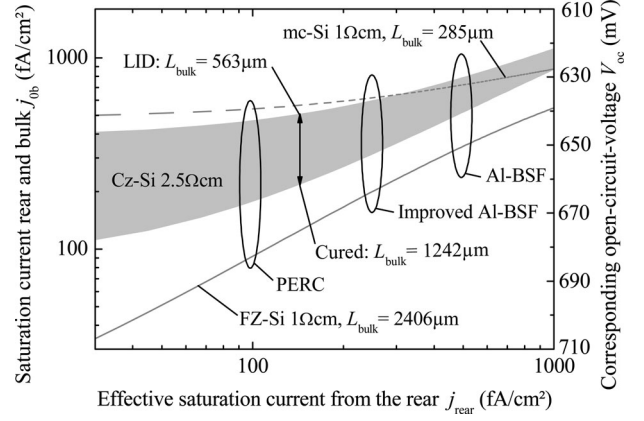


Fig. 7. Saturation current of the rear and the bulk j_{0b} in dependence of the saturation current of the rear j_{rear} is shown. Typical bulk lifetimes for silicon and doping densities are incorporated. For Cz-Si, light-induced degraded (LID) lifetime according to Bothe *et al.* [27] and a “cured” value of $\tau = 400 \mu s$ is used.

In Fig. 7, typical j_{0b} values for p-type silicon-based solar cells for typical effective dark saturation currents at the rear j_{rear} are shown.

However, the corresponding areas only serve as guidelines, since they depend on technological aspects and surface preparation of the bulk material incorporated.

C. Nonideal Recombination

The expression “nonideal recombination” combines recombination mechanisms that lead to ideality factors greater than one. This generates a kink [28] visible in the logarithmic plotted dark $I-V$ or suns $-V_{oc}$ curve [29] which, in most cases, influences the maximum power point of a solar cell device.

In order to model losses associated with nonideal recombination, the quantity j_{02} has been introduced by Sah *et al.* [7] and Nussbaum [30]. They derived an ideality factor of $n = 2$ by assuming a single mid-gap defect state associated with a contamination of the silicon material. The authors assume a penetration of impurities during contact sintering through the emitter layer to the depletion region. The following procedure for the determination of j_{02} has been used:

- 1) calculation of j_{01} out of the quantities j_{0e-n+} and j_{0e-met} , priority determined in Section III-A in this paper;
- 2) generation of the $I-V$ curve by means of the one-diode model;
- 3) addition of the second exponential term associated to j_{02} with a constant ideality factor of $n = 2$ until the corresponding fill factor matches the measured suns $-V_{oc}$ fill factor pFF .

The advantage of the present model corresponds to its simplicity ignoring physical effects that might increase the ideality factor to 2 or beyond [28], [31]–[34]. The fill factor losses are regarded as effective quantities in the values j_{02} and j_{02-met} . Note that this analysis has been conducted for negligible shunt current. At present shunt, the leakage current at maximum power point also needs to be considered.

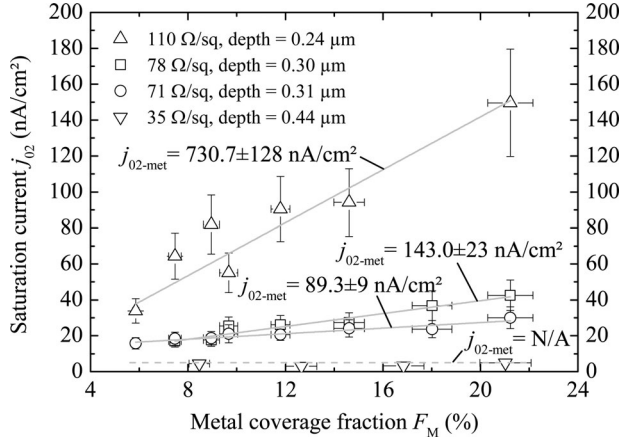


Fig. 8. Recombination current j_{02} is plotted in dependence of the metal coverage for different emitter sheet resistances. The depth of the profile corresponds to a doping level of 10^{17} cm^{-3}

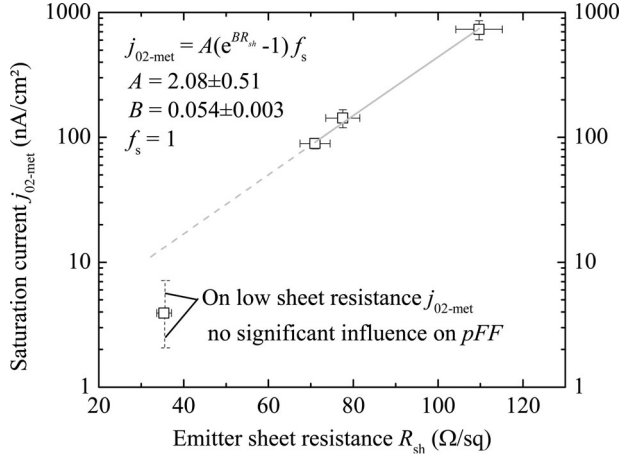


Fig. 9. Extracted $j_{02\text{-met}}$ is plotted versus the corresponding emitter sheet resistance. The value for the 35-Ω/sq emitter is obtained by averaging values given in Fig. 8. It shall demonstrate the strong decrease of $j_{02\text{-met}}$ with decreasing emitter sheet resistance. Therefore, the extracted fit-function indicated by the dashed line serves as upper bound. The factor f_s enables a scaling of the resulting parameterization of $j_{02\text{-met}}$.

Due to the chosen approach, the authors assume a constant j_{02} for effectively passivated emitter regions leading to $j_{02} = j_{02\text{-n}^+} = j_{02\text{-n}^{++}}$.

In Fig. 8, the effective saturation current j_{02} is plotted versus the metal coverage fraction F_M on different emitters. As can be seen in the figure, j_{02} scales with the emitter sheet resistance and thus with the depths of the emitter corresponding to the location of the depletion region. In order to separate the influence of the emitter-metal contact on j_{02} from other influencing quantities, the expression $j_{02\text{-met}}$ is introduced in (3).

The emitter with a sheet resistance of 35 Ω/sq shows hardly any significant slope; therefore, it shows a disappearing $j_{02\text{-met}}$.

Fitting the values extracted with (3) relates $j_{02\text{-met}}$ to the emitter sheet resistance and leads to an empirical model shown in Fig. 9. The strong influence of R_{sh} on $j_{02\text{-met}}$ supports the approach of the contaminated depletion region by the front electrode. In the case of nickel seed-layer approaches, this behavior is already known [35].

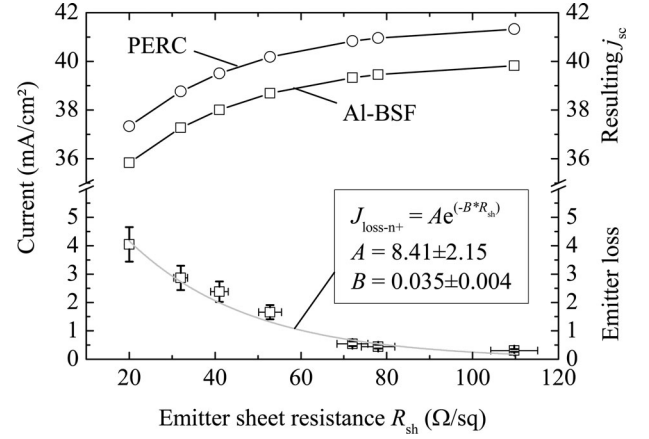


Fig. 10. Experimentally obtained loss in photogenerated current due to emitter recombination in dependence of the emitter sheet resistance in the lower section of the graph is displayed. For the solar cell with a full-area Al-BSF, the maximum photogenerated current is limited at 40 mA/cm²; however, for a PERC device with superior rear reflectance, the limit reaches 41.5 mA/cm².

Note that the obtained parameterization of $j_{02\text{-met}}$ is influenced by the fixed ideality factor of $n = 2$. In addition, it is likely that due to mentioned effects, a voltage independent n or j_0 cannot always be found. Furthermore, we observe a strong dependence of the firing temperature and chosen paste on pFF . Therefore, we introduce a scaling factor f_s , that is initially set to $f_s = 1$ and accounts for the strong diversity and dependences of this parameter. A more detailed analysis regarding paste and temperature dependence is published by Hoenig *et al.* [12].

D. Photogenerated Current

The so-called blue-response is strongly influenced by the amount of phosphorus incorporated in the front highly doped region [36]. In order to obtain an analytical model, we relate the emitter sheet resistance to the photogenerated current, as demonstrated in Fig. 10. A dead-layer model introduced in Fischer's Ph.D. dissertation [37] enables the separation of emitter and bulk losses in the internal quantum efficiency. This model has been implemented by Thaidigsmann *et al.* [38] and experimentally verified by Jäger *et al.* [39].

The upper curves in Fig. 10 show the limit in photogenerated current in dependence of R_{sh} for two different rear-side concepts.

As can be seen, the photogenerated loss in the emitter region is inversely proportional to the emitter sheet resistance. In case of a full-area Al-BSF, the maximum photogenerated current reaches 40 mA/cm². However, for a PERC device with superior rear properties, the limit reaches 41.5 mA/cm². These values strongly depend on cell thickness and optical properties of both front and rear side and, therefore, have to be determined individually. These limits have been obtained by applying an analytical model presented in [37], taking into account carrier lifetime, thickness, and optical properties of the bulk and rear. Free carrier absorption of near-bandgap light in the emitter region is not taken into account here. An additional implementation is doable and can be found in [40].

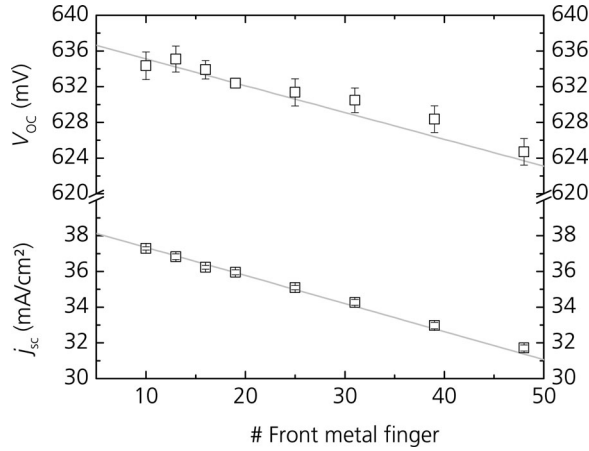


Fig. 11. Open-circuit voltage V_{oc} and the short-circuit current j_{sc} measured and simulated are shown. The median value from six solar cells corresponds to one data point.

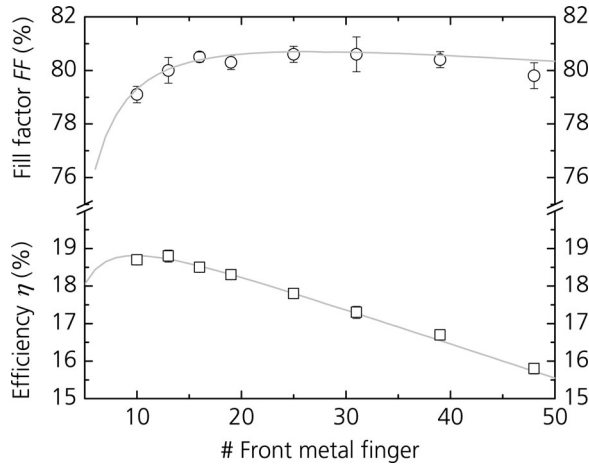


Fig. 12. Fill factor FF and the conversion efficiency η measured and simulated are shown. The median value from six solar cells corresponds to one data point.

IV. RESULTS

Using the parameter set presented in Section III in “Gridmaster,” very good agreement is obtained between the measured and the simulated data. The measured I – V data for the solar cell device presented in Section III are shown in Figs. 11 and 12. V_{oc} decreases due to the increased area of the unpassivated emitter and decreasing j_{sc} . Publications from Cuevas and Lopez-Romero [41] and Greulich *et al.* [42] report decreasing V_{oc} , with increasing influence of resistive losses. The effect is related to the distributed series resistance of a solar cell and enhanced by high j_{0e-met} values. It seems for ten or lower grid fingers this behavior is on setting. However, for solar cells with a typical series resistance of around $1 \Omega \cdot \text{cm}^2$ or less, this effect is of minor magnitude.

As can be seen, measured and simulated efficiency are in good accordance.

Additionally, in Table I, further input parameters are displayed. An effective finger height refers to a rectangle with the same cross-sectional area compared with the original shape.

TABLE I
IN ADDITION TO THE PARAMETERS PRESENTED IN SECTION III, FURTHER EXPERIMENTALLY OBTAINED PARAMETERS ARE UTILIZED

Solar cell	$2 \times 2 \text{ cm}^2$, Si-FZ
Effective finger height	$9.1 \mu\text{m}$
Finger width	$85 \mu\text{m}$
Busbar width	$197 \mu\text{m}$
Paste resistivity	$5 \mu\Omega\text{cm}$
Emitter sheet resistance	$71 \Omega/\text{sq}$
Contact resistivity	$3.3 \Omega\text{cm}^2$

The effective finger height has been obtained as quotient of the cross-sectional area and the finger width. The contact resistivity is measured by means of the TLM approach [43].

V. CONCLUSION

In this paper, an Excel-based analytical tool named Gridmaster has been presented, allowing the fast analytical modeling of conventional and MWT solar cells.

A detailed characterization relates important input parameters required for the simulation of conventional and MWT solar cells to the emitter sheet resistance. Those parameters include the dark saturation current of the passivated and metallized emitter area, nonideal recombination expressed as an effective dark saturation current with an ideality factor of 2, and the photogenerated current for full-area alloyed Al and PERC devices.

As a remarkable result is the distinguished correlation between sheet resistance and nonideal recombination, it has been experimentally shown that solar cells with a lowly doped emitter under the front electrode exhibit an increased recombination, which affects both the open-circuit voltage and the fill factor. Both loss mechanisms are expressed in the dark saturation current densities j_{0e-met} and j_{02-met} . Regarding the latter, the authors show the impact of a metal contaminated depletion region for a sintered front electrode. This quantity is strongly related to the emitter profile, the screen-printing paste, and sintering conditions and has to be considered individually.

APPENDIX A

SERIES RESISTANCE IN CONVENTIONAL SOLAR CELLS

The “lumped series resistance” approach for modeling the power drop due to resistive losses is well known and described in the standard references [13], [14]. The idea is based on the reduction of the device to its smallest periodical structure—the elementary or unit cell. Due to the periodicity, physical properties in one single unit are extendable to the whole device. In Fig. 13, one of the possible unit cell designs is emphasized. It enfolds half of the BB-BB distance including one grid finger and a BB segment.

1) Series Resistance of the Emitter

During operation under illumination, electrons are assumed to be injected homogeneously in the emitter. Therefore, the electron flow in the unit cell increases linearly toward the edge of a grid finger. This assumption leads to following expression for the

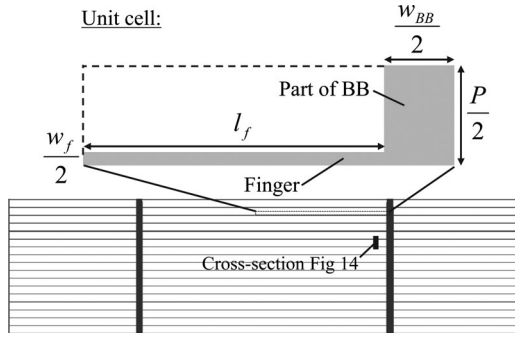


Fig. 13. Typical front grid of a conventional solar cell is displayed. Enlarged is one possible unit cell for this kind of grid structure.

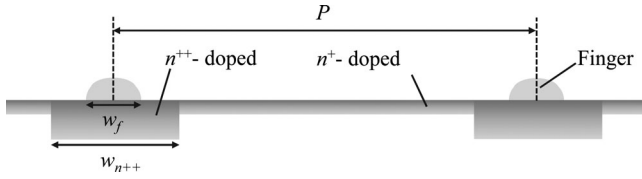


Fig. 14. Cross section as indicated in Fig 13 is shown.

series resistance caused by the emitter:

$$r_E = \frac{1}{6} \cdot R_{sh} \cdot \frac{(P - w_f)}{l_f} \cdot A_{EZ-I}, A_{EZ-I} = \frac{P}{2} \cdot \left(l_f + \frac{w_{BB}}{2} \right) \quad (5)$$

whereby R_{sh} is the sheet resistance of the emitter. This expression neglects electrons that are collected by the busbar.

In order to account for a selective emitter, the expression for the series resistance needs to be extended to account for the current flow through the highly doped emitter area n^{++} .

According to the cross-section indicated in Figs. 13 and 14, the expression for the lowly doped part reads:

$$r_{E-n^{+}} = \frac{1}{6} \cdot R_{sh-n^{+}} \cdot \frac{(P - w_{n^{++}})}{l_f} \cdot A_{EZ-I}. \quad (6)$$

For the highly doped region, a more complex equation is obtained. The power loss PW in this area reads

$$PW_{E-n^{++}} = \frac{1}{3} \cdot \frac{R_{sh-n^{++}}}{j_{ph-n^{++}} \cdot l_f^2} \cdot \left(\left(I_{ph-n^{++}} + j_{ph-n^{++}} \cdot \frac{l_f}{2} \cdot (w_{n^{++}} - w_f) \right)^3 - I_{ph-n^{++}}^3 \right). \quad (7)$$

An expression for the series resistance is obtained by dividing (7) with the square of the maximum current I_{max}^2 flowing through the highly doped emitter

$$r_{E-n^{++}} = \frac{PW_{E-n^{++}}}{I_{max}^2} A_{EZ-I}$$

$$I_{max} = j_{ph-n^{++}} \cdot \frac{l_f}{2} \cdot (P - w_{n^{++}}) + j_{ph-n^{++}} \cdot \frac{l_f}{2} \cdot (w_{n^{++}} - w_f). \quad (8)$$

Contrary to the lowly doped case, this expression depends on the currents generated throughout the whole emitter area. In order to obtain an analytical equation, the apparent exter-

nal current $j(V)$ is substituted by the photogenerated currents $j_{ph-n^{++}(+)}$. This approach leads to a small overestimation of the series resistance in the n^{++} -emitter.

2) Series Resistance of the Front Metal Grid

Along the grid finger toward the busbar, the electron flow increases linearly; therefore, the expression for the series resistance in the grid finger reads

$$r_f = \frac{2}{3} \cdot \rho_f \cdot \frac{l_f}{w_f \cdot h_{f-eff}} \cdot A_{EZ-I}. \quad (9)$$

whereby ρ_f represents the specific resistance of the grid fingers and h_{f-eff} the effective height corresponding to a grid finger with a rectangular cross section.

Losses due to current flow in the busbar depend on the external contact geometry. Usually, an array of pin-pairs is utilized for current and voltage contacting each busbar homogenously. Therefore, the expression for the series resistance occurring in the busbar reads

$$r_{BB} = \frac{1}{3} \cdot \rho_{BB} \cdot \frac{w_c}{2 \cdot n_{pins-BB} \cdot h_{BB} \cdot w_{BB}} \cdot A_{EZ-II}$$

$$A_{EZ-II} = \frac{w_c \cdot l_c}{2 \cdot n_{pins-BB} \cdot n_{BB}}. \quad (10)$$

whereby b_c/l_c is the width/length ratio of the whole cell, h_{bb}/w_{BB} is the height/width ratio of the busbar, $n_{pins-BB}$ is the quantity of current pins contacting one busbar, and n_{BB} is the quantity of busbars.

It is assumed that half of the current pin-to-pin distance along the busbar is much larger than the grid finger pitch.

3) Contact Resistance of the Silicon-Metal Interface

For the contact resistance, the following expression is used:

$$r_c = \frac{\rho_c}{\left(\left(l_f + \frac{1}{2} (P - w_f) \right) \cdot L_T \right)} \cdot \coth \left(\frac{w_f}{2 \cdot L_T} \right) \cdot A_{EZ-I}$$

$$L_T = \sqrt{\frac{\rho_c}{R_{sh-n^{++}(+)}}} \quad (11)$$

whereby ρ_c is the specific contact resistance, and L_T is the transfer length. Due to the nonlinear hyperbolic cotangent in (11), the choice of the unit cell is restricted to the size as defined in (5). Furthermore, l_f is extended by P in order to take into account current collection by the busbar that slightly reduces the resulting contact resistance.

4) Series Resistance of the Bulk

For the expression of the series resistance in the bulk, it is assumed that photogeneration exists only at the front side. Therefore, all holes reaching the rear side propagate through the total thickness of the device. Hence, following equation for the series resistance in the bulk holds for the upper limit:

$$r_B = \rho_B \cdot W \quad (12)$$

whereby ρ_B is the specific resistivity of the bulk silicon and W the thickness of the device.

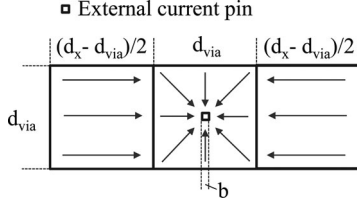


Fig. 15. Idealized current flow pattern within a unit cell of the rear side toward an external current pin is displayed. The unit cell is divided in two areas: a rectangular shaped ("rec") region where current is assumed to flow in parallel and a square region ("sq") located around the external current pin where radial current flow is assumed.

5) Series Resistance of the Rear Electrode

The current flow through the rear electrode depends on the external contact geometry. In the most cases, the external contact of the fully metallized rear side is realized by an array of pins opposing the array contacting the front n -contact. Therefore, the following assumption holds $n_{\text{BB-front}} = n_{\text{Pad-rear}} = n_{\text{BB}}$. In order to account for the 2-D current flow, an approach commonly used for the front side of EWT [44] solar cells is taken.

In this section, all following equations are based on [45] and has been extended by Fallisch *et al.* [46]

$$r_{\text{sq}} = \frac{R_{\text{Sh-Al}} \cdot d_{\text{via}}^2}{2 \cdot \pi} \cdot \left(\ln \left(\frac{d_{\text{via}}}{b} \right) - \frac{3}{4} + \frac{b^2}{d_{\text{via}}^2} - \frac{b^4}{4d_{\text{via}}^4} \right) \cdot \left(1 + \frac{d_x - d_{\text{via}}}{d_{\text{via}}} f \right). \quad (13)$$

Equation (13) takes into account a radially symmetric current flow pattern within the square around the external current pin and introduces correction factors for compensation of deviations from radial symmetry. The empiric factor f compensates for the current flowing only through two sides of the square. The assumed current flow pattern is shown in Fig. 15.

The following equation is taking into account parallel current flow in the rectangular part of the unit cell. This equation has been modified compared with its literature form in order to maintain monotonous decreasing behavior of (15) toward vanishing d_{via} :

$$r_{\text{rec}} = \frac{1}{12} \cdot R_{\text{sh-Al}} \cdot d_x^2. \quad (14)$$

Finally, (15) yields the losses associated with the current flow through the rear metallization of a solar cell

$$r_{\text{s-Al}} = r_{\text{sq}} + r_{\text{rec}}. \quad (15)$$

Fig. 16 displays the series resistance for the rear metallization according to (15). For $d_{\text{via}} = 0$ ($n_{\text{pin-Al}} = \text{inf.}$), (13), vanishes, and $r_{\text{s-Al}} = r_{\text{rec}}$.

APPENDIX B

METAL-WRAP-THROUGH-RELATED LOSSES

The MWT approach enables a higher efficiency potential compared with the conventional solar cell architecture. In contrary, series resistance losses are more pronounced due to additional contributions [17].

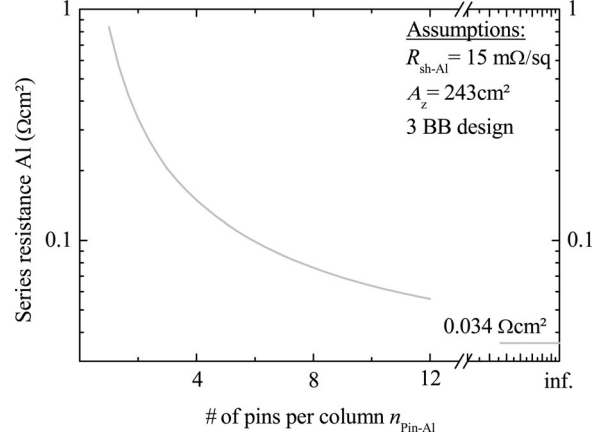


Fig. 16. Series resistance according to (15) is displayed. For vanishing d_{via} ($n_{\text{pin-Al}} = \text{inf.}$), (13) vanishes, and (15) converges into (14).

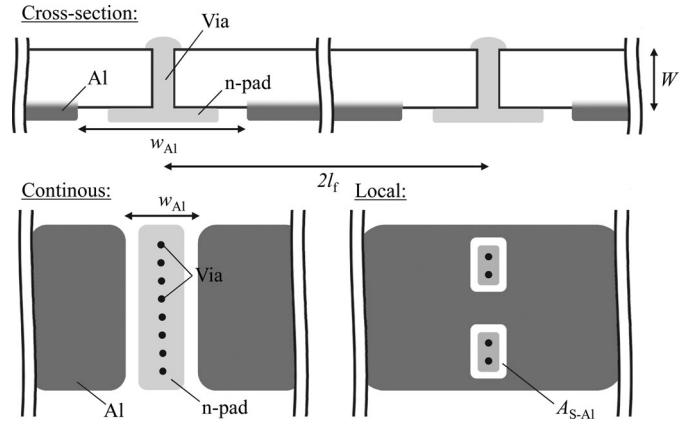


Fig. 17. Cross section and two possible rear designs of an MWT solar cell are drawn.

1) Series Resistance of the Via Through Metallization

All vias (n_{via}) connect the front electrode to the rear pads in parallel. Therefore, by assuming a homogenous distribution of vias and an average via resistance R_{via} , the weighted contribution is obtained as follows:

$$r_{\text{via}} = \frac{R_{\text{via}}}{n_{\text{via}}} \cdot w_c \cdot l_c. \quad (16)$$

2) Lateral Series Resistance of the Bulk

A geometrically inspired approach leads so a simple analytical equation of the lateral series resistance in the bulk [17]

$$r_{\text{Lat-cont}} = \frac{1}{24} \cdot \rho_B \cdot \frac{w_{\text{Al}}^3}{W \cdot l_f}. \quad (17)$$

Equation (17) assumes a continuous n -pad on the rear side, as outlined in Fig. 17 on the left side.

In order to increase the coverage fraction of the electrically positive area, continuous n -pads are substituted by local structures as demonstrated in Fig. 17 on the right side. Therefore, the area of the opening in the p -contact for one local n -pad is assumed to exhibit a radial symmetry with the radius R_o . Current flows radially from the origin of the circle toward the

p -contact and increases linearly. Hence, the lateral series resistance $r_{\text{Lat-Loc}}$ induced by a local n -pad with respect to the standard “power-loss-approach” reads

$$\begin{aligned} d\text{PW}_{\text{Lat-Loc}} &= I^2 \cdot dR = (j\pi r_o^2)^2 \cdot \rho_B \frac{dr_o}{2\pi r_o W} \\ \text{PW}_{\text{Lat-Loc}} &= \rho_B \frac{j^2 \pi}{2W} \cdot \int_0^{R_o} r_o^3 dr_o = \rho_B \frac{j^2 \pi R_o^4}{8W} \\ R_{\text{Lat-Loc}} &= \frac{P}{(j\pi R_o^2)^2} = \frac{\rho_B}{8\pi W} \\ r_{\text{Lat-Loc}} &= R_{\text{Lat-Loc}} \cdot \underbrace{A_{\text{s-Al}}}_{\text{EZ}} \cdot \underbrace{\frac{n_{\text{Loc}}}{w_c \cdot l_c}}_{\text{weighting}} \\ &= \rho_B \cdot \frac{\pi R_o^4}{8W} \cdot \frac{n_{\text{Loc}}}{w_c \cdot l_c} \end{aligned} \quad (18)$$

whereby n_{Loc} is the total quantity of local n -pads on the rear side. Lateral current in the base due to solder p -pads is accounted for the same way. Note that the unit cell $A_{\text{s-Al}}$ is no periodic element of the solar cell. Therefore, its contribution to the lumped series resistance needs to be weighted with a periodic element that includes the chosen unit cell [(17) is obtained the same way].

Note that the solder pads providing the p -contact for both conventional and MWT solar cell might also induce an area of lateral current flow in the bulk and depending on geometry treated as defined in (17) or (18).

3) Series Resistance in the Rear N -Pad

In the case of a continuous n -pad, current flows toward the next accessible external current pin providing the same loss as in a case of a front busbar. Therefore, (10) holds if adapted to respective geometry and resistivity.

In case of local n -pads, current is transferred by the grid fingers to the pseudobusbar on the front side of the MWT solar cell and is treated as a series resistance of a busbar on the front side.

ACKNOWLEDGMENT

The authors would like to thank S. Glunz, D. Huljić, M. Hörteis, and A. Mette for their pioneering involvement on the tool presented in this work; Prof. Willeke and Prof. Clement for their fruitful discussion; and, finally, the whole PV-TEC team for processing and characterization.

REFERENCES

- [1] Sentaurus TCAD, “Release E-2010.12,” ed. Zürich, Switzerland: Synopsis, 2010.
- [2] *ATLAS, Atlas User Manual 2013*, ed. Santa Clara, CA, USA: Silvaco.
- [3] K. Rapolu, P. Singh, and S. P. Shea, “Two dimensional numerical modeling of a silicon solar cell with deep contacts in the emitter,” in *Proc. 34th IEEE Photovoltaic Spec. Conf.*, Philadelphia, PA, USA, 2009, pp. 1048–1053.
- [4] L. W. Nagel and D. O. Pederson, “Simulation program with integrated circuit emphasis (SPICE),” in *Proc. 16th Midwest Symp. Circuit Theory*, Waterloo, ON, Canada, 1973, pp. 1–65.
- [5] E. van Kerschaver, R. Einhaus, J. Szlufcik, J. Nijs, and R. Mertens, “A novel silicon solar cell structure with both external polarity contacts on the back surface,” in *Proc. 2nd World Conf. Photovoltaic Energy Convers.*, Vienna, Austria, 1998, pp. 1479–1482.
- [6] W. Shockley, “The theory of p - n junctions in semiconductors and p - n junction transistors,” *Bell Syst. Tech. J.*, vol. 28, pp. 435–489, 1949.
- [7] C. T. Sah, R. N. Noyce, and W. Shockley, “Carrier generation and recombination in p - n junctions and p - n junction characteristics,” *Proc. IRE*, vol. 45, pp. 1228–1243, 1957.
- [8] W. Shockley and W. T. J. Read, “Statistics of the recombinations of holes and electrons,” *Phys. Rev.*, vol. 87, pp. 835–842, 1952.
- [9] R. R. King, P. E. Gruenbaum, R. A. Sinton, and R. M. Swanson, “Passivated emitters in silicon solar cells,” in *Proc. 21st IEEE Photovoltaic Spec. Conf.*, Kissimmee, FL, USA, 1990, pp. 227–232.
- [10] A. Cuevas, P. A. Basore, G. Girault-Matlakowski, and C. Dubois, “Surface recombination velocity of highly doped n -type silicon,” *J. Appl. Phys.*, vol. 80, pp. 3370–3375, 1996.
- [11] M. J. Kerr, J. Schmidt, A. Cuevas, and J. H. Bultman, “Surface recombination velocity of phosphorus-diffused silicon solar cell emitters passivated with plasma enhanced chemical vapor deposited silicon nitride and thermal silicon oxide,” *J. Appl. Phys.*, vol. 89, pp. 3821–3826, 2001.
- [12] R. Hoenig, A. Kalio, J. Sigwarth, F. Clement, M. Glatthaar, J. Wilde, and D. Biro, “Impact of screen printing silver paste components on the space charge region recombination losses of industrial silicon solar cells,” *Solar Energy Mater. Solar Cells*, vol. 106, pp. 7–10, 2012.
- [13] A. Goetzberger, B. Voß, and J. Knobloch, *Sonnenenergie: Photovoltaik*. Stuttgart, Germany: Teubner Studienbücher Physik, 1994.
- [14] M. A. Green, *Third Generation Photovoltaics: Advanced Solar Energy Conversion*. New York, NY, USA: Springer, 2003.
- [15] A. Cuevas and R. A. Sinton, “Detailed modelling of silicon solar cells,” in *Proc. 23rd Eur. Photovoltaic Solar Energy Conf.*, Valencia, Spain, 2008, pp. 315–319.
- [16] F. Clement, M. Lutsch, T. Kubera, M. Kasemann, W. Kwapil, C. Harmel, N. Mingirulli, D. Erath, H. Wirth, D. Biro, and R. Preu, “Processing and comprehensive characterisation of screen-printed mc-Si metal wrap through (MWT) solar cells,” in *Proc. 22nd Eur. Photovoltaic Solar Energy Conf.*, Milan, Italy, 2007, pp. 1399–1402.
- [17] F. Clement, M. Menkoe, T. Kubera, C. Harmel, R. Hoenig, W. Wolke, H. Wirth, D. Biro, and R. Preu, “Industrially feasible multi-crystalline metal wrap through (MWT) silicon solar cells exceeding 16% efficiency,” *Solar Energy Mater. Solar Cells*, vol. 93, pp. 1051–1055, 2009.
- [18] K. Meyer, H.-J. Krokoszinski, D. Lahmer, T. Wuetherich, M. Dupke, R. Jesswein, J. Lossen, P. Zerrer, and A. Prießner, “Novel MWT cell design on monocrystalline silicon wafers,” in *Proc. 25th Eur. Photovoltaic Solar Energy Conf. Exhib.*, Valencia, Spain, 2010, pp. 1774–1777.
- [19] I. G. Romijn, A. A. Mewe, M. W. P. E. Lamers, E. Kossen, E. E. Bende, and A. W. Weeber, “An overview of MWT cells and evolution to aspire concept: A new integrated mc-Si cell and module design for high efficiencies,” in *Proc. 23rd Eur. Photovoltaic Solar Energy Conf.*, Valencia, Spain, 2008, pp. 1–6.
- [20] G. Hahn, “Status of selective emitter technology,” in *Proc. 25th Eur. Photovoltaic Solar Energy Conf. Exhib.*, Valencia, Spain, 2010, pp. 1091–1096.
- [21] U. Jäger, S. Mack, A. Kimmerle, A. Wolf, and R. Preu, “Influence of doping profile of highly doped regions for selective emitter solar cells,” in *Proc. 35th IEEE Photovoltaic Spec. Conf.*, Honolulu, HI, USA, 2010.
- [22] J. Greulich, U. Jäger, S. Rein, and R. Preu, “A review and comparison of one- and two-dimensional simulations of solar cells featuring selective emitters,” *IEEE J. Photovoltaics*, vol. 2, no. 4, pp. 1–9, Oct. 2012.
- [23] T. Fellmeth, A. Born, A. Kimmerle, F. Clement, D. Biro, and R. Preu, “Recombination at metal-emitter interfaces of front contact technologies for highly efficient silicon solar cells,” in *Proc. 1st Int. Conf. Silicon Photovoltaics*, Freiburg, Germany, 2011, pp. 115–121.
- [24] D. E. Kane and R. M. Swanson, “Measurement of the emitter saturation current by a contactless photoconductivity decay method (silicon solar cells),” in *Proc. 18th IEEE Photovoltaic Spec. Conf.*, Las Vegas, NV, USA, 1985, pp. 578–583.
- [25] A. L. Fahrenbruch and R. H. Bube, *Fundamentals of Solar Cells*. New York, NY, USA: Academic, 1983.
- [26] J. Krause, R. Woehl, and D. Biro, “Analysis of local Al- p^+ -layers for solar cells processed by small screen-printed structures,” in *Proc. 25th Eur. Photovoltaic Solar Energy Conf. Exhib.*, Valencia, Spain, 2010, pp. 1899–1904.
- [27] K. Bothe, R. Hezel, and J. Schmidt, “Recombination-enhanced formation of the metastable boron-oxygen complex in crystalline silicon,” *Appl. Phys. Lett.*, vol. 83, pp. 1125–1127, 2003.
- [28] K. R. McIntosh, “Lumps, humps and bumps: Three detrimental effects in the current-voltage curve of silicon solar cells,” Ph.D. dissertation, Cent. Photovoltaic Eng., Univ. New South Wales, Sydney, Australia, 2001.

- [29] R. A. Sinton and A. Cuevas, "A quasi-steady-state open-circuit voltage method for solar cell characterization," in *Proc. 16th Eur. Photovoltaic Solar Energy Conf.*, Glasgow, U.K., 2000, pp. 1152–1155.
- [30] A. Nussbaum, "Generation-recombination characteristic behaviour of silicon diodes," *Physica Status Solidi A*, vol. 19, pp. 441–450, 1973.
- [31] A. Schenk and U. Krumbein, "Coupled defect-level recombination: Theory and application to anomalous diode characteristics," *J. Appl. Phys.*, vol. 78, pp. 3185–3192, 1995.
- [32] O. Breitenstein, J. Bauer, A. Lotnyk, and J.-M. Wagner, "Defect induced non-ideal dark I-V characteristics of solar cells," *Superlattices Microstructures*, vol. 45, pp. 182–189, 2008.
- [33] B. T. Michl, M. Rüdiger, J. A. Giesecke, M. Hermle, W. Warta, and M. C. Schubert, "From injection dependent lifetime to solar cell efficiency," in *Proc. 26th Eur. Photovoltaic Solar Energy Conf. Exhib.*, Hamburg, Germany, 2011, pp. 1058–1062.
- [34] S. R. Wenham, S. J. Robinson, X. Dai, J. Zhao, A. Wang, Y. H. Tang, A. Ebong, C. B. Honsberg, and M. A. Green, "Rear surface effects in high efficiency silicon solar cells," in *Proc. 1st World Conf. Photovoltaic Energy Convers.*, Waikoloa, HI, USA, 1994, pp. 1278–1282.
- [35] J. Bartsch, A. Mondon, B.-J. Godejohann, M. Hörteis, and S. W. Glunz, "Advanced front side metallization for crystalline silicon solar cells based on a fully plated contact," in *Proc. 25th Eur. Photovoltaic Solar Energy Conf. Exhib.*, Valencia, Spain, 2010, pp. 1978–1983.
- [36] G. Masetti, M. Severi, and S. Solmi, "Modeling of carrier mobility against carrier concentration in arsenic-doped, phosphorus-doped, and boron-doped silicon," *IEEE Trans. Electron Devices*, vol. ED-30, no. 7, pp. 764–769, Jul. 1983.
- [37] B. Fischer, "Loss analysis of crystalline silicon solar cells using photo-conductance and quantum efficiency measurements," Ph.D. dissertation, Fachbereich Physik, Univ. Konstanz, Konstanz, Germany, 2003.
- [38] B. Thaidigsmann, A. Wolf, and D. Biro, "Accurate determination of the IQE of screen printed silicon solar cells by accounting for the finite reflectance of metal contacts," in *Proc. 24th Eur. Photovoltaic Solar Energy Conf.*, Hamburg, Germany, 2009, pp. 2056–2059.
- [39] U. Jäger, B. Thaidigsmann, M. Okanovic, and R. Preu, "Quantum efficiency analysis of highly doped areas form selective emitter solar cells," in *Proc. 1st Int. Conf. Silicon Photovoltaics*, Freiburg, Germany, 2011, pp. 193–199.
- [40] D. A. Clugston and P. A. Basore, "Modelling free-carrier absorption in solar cells," *Progr. Photovoltaics: Res. Appl.*, vol. 5, pp. 229–236, 1997.
- [41] A. Cuevas and S. Lopez-Romero, "The combined effect of non-uniform illumination and series resistance on the open-circuit voltage of solar cells," *Solar Cells*, vol. 1984, pp. 163–173, 1984.
- [42] J. Greulich, M. Glatthaar, A. Krieg, G. Emanuel, and S. Rein, "JV characteristics of industrial silicon solar cells: Influence of distributed series resistance and shockley read hall recombination," in *Proc. 24th Eur. Photovoltaic Solar Energy Conf.*, Hamburg, Germany, 2009, pp. 2065–2069.
- [43] H. H. Berger, "Contact resistance and contact resistivity," *J. Electrochem. Soc.*, vol. 119, pp. 507–514, 1972.
- [44] J. M. Gee, W. K. Schubert, and P. A. Basore, "Emitter wrap-through solar cell," in *Proc. 23rd IEEE Photovoltaic Spec. Conf.*, Louisville, KY, USA, 1993, pp. 265–270.
- [45] R. N. Hall and T. J. Soltys, "Polka dot solar cell," in *Proc. 14th IEEE Photovoltaic Spec. Conf.*, San Diego, CA, USA, 1980, pp. 550–553.
- [46] A. Fallisch and D. Biro, "2-D SPICE simulation and analytical calculation of spreading resistance effects in emitter wrap-through cells with nonsquare via-hole pattern," *IEEE J. Photovoltaics*, vol. 1, no. 2, pp. 153–158, Oct. 2011.

Authors' photographs and biographies not available at the time of publication.